

A Transiting Giant on a 7.7-Year Orbit Revealed by TTVs in the TOI-201 System

GRACJAN MACIEJEWSKI ¹ AND WERONIKA LOBODA¹

¹*Institute of Astronomy, Faculty of Physics, Astronomy and Informatics, Nicolaus Copernicus University in Toruń, Grudziadzka 5, 87-100 Toruń, Poland*

(Received June 23, 2025; Accepted July 14, 2025)

Submitted to ApJL

ABSTRACT

We report the detection and characterization of TOI-201 c, a long-period transiting companion to the warm Jupiter TOI-201 b. Its presence was first inferred from high-amplitude transit timing variations (TTVs) in TOI-201 b, pointing to a massive outer body on a $7.7^{+1.0}_{-0.6}$ -year eccentric orbit. This prediction was confirmed when TESS observed a transit of TOI-201 c, precisely constraining its orbital geometry. A joint fit to TTVs, transit photometry, and archival radial velocities yields a mass of $14.2^{+1.0}_{-1.2} M_{\text{Jup}}$ and an eccentricity of $0.643^{+0.009}_{-0.021}$. The mutual inclination between planets b and c is $2.9^{+4.8}_{-4.4}$ degrees, indicating a nearly coplanar architecture. Long-term numerical integrations confirm dynamical stability over gigayear timescales and predict that transits of TOI-201 b will cease within a few thousand years. TOI-201 c ranks among the longest-period transiting planets with well-constrained properties. Its detection via TTVs, followed by a confirmed transit, represents a rare observational sequence and highlights the power of TTVs and photometric monitoring to uncover distant companions. The TOI-201 system offers a valuable laboratory for testing models of giant planet formation, migration, and secular evolution in multi-planet systems.

Keywords: Exoplanets (498) — Exoplanet dynamics (490) — Transit photometry (1709) — Transit timing variation method (1710) — Radial velocity (1332)

1. INTRODUCTION

The star TOI-201 (HD 39474, HIP 27515) is an F6–7 dwarf (N. Houk & A. P. Cowley 1975; M. J. Hobson et al. 2021). Two candidate transiting planets were identified in its light curve, obtained by the *Transiting Exoplanet Survey Satellite* (TESS; G. R. Ricker et al. 2015), and reported by N. M. Guerrero et al. (2021). The deeper signal corresponds to TOI-201 b, showing a transit-like feature with a period $P_b \approx 53$ d, depth ≈ 6 ppth, and duration ≈ 280 minutes (M. Montalto et al. 2020; N. M. Guerrero et al. 2021; J. Dong et al. 2021). M. J. Hobson et al. (2021) confirmed its planetary nature and determined a mass of $M_b = 0.42^{+0.05}_{-0.03} M_{\text{Jup}}$ and a radius of $R_b = 1.008^{+0.012}_{-0.015} R_{\text{Jup}}$, with an eccentric orbit ($e_b = 0.28^{+0.06}_{-0.09}$) and semi-major axis $a_b = 0.30^{+0.02}_{-0.03}$ au. In addition to the planet’s induced radial velocity signal, M. J. Hobson et al. (2021) also reported a long-

term trend, initially attributed to stellar activity based on its complexity and the star’s estimated young age of $0.87^{+0.46}_{-0.49}$ Gyr.

The second candidate, TOI-201.02, may be a $1.7 R_{\oplus}$ planet in a 5.8-day orbit (N. M. Guerrero et al. 2021), though its planetary status remains unconfirmed by follow-up observations (M. J. Hobson et al. 2021).

Thanks to its long orbital period and coverage across multiple TESS sectors, TOI-201 b was included in our program to search for short-period transit timing variations (TTVs), which may signal the presence of exomoons perturbing their host planets (D. Kipping 2021). Transits observed during TESS Cycles 1 and 3 were consistent with a linear ephemeris. However, this changed with the inclusion of three transits from Cycle 5, which revealed an apparent increase in TOI-201 b’s orbital period (W. Loboda 2024). This unexpected deviation prompted a deeper investigation of the system, ultimately leading to the detection of an additional massive, transiting companion in a wider orbit—a discovery we present in this Letter.

2. TESS OBSERVATIONS

TOI-201 lies approximately 12° from the southern ecliptic pole, near the edge of the TESS Southern Continuous Viewing Zone. As a result, the system was monitored almost continuously during Cycles 1, 3, and the first half of Cycle 5. To date, it has been observed in 32 sectors with a two-minute cadence, yielding complete transits of TOI-201 b in 15 of them.

We used the `Lightkurve v2.0` package (Lightkurve Collaboration et al. 2018) to extract light curves via aperture photometry from the two-minute cadence target pixel files. For sectors contaminated by background scattered light, we applied the `RegressionCorrector` module to enhance photometric precision. Transits were masked using 15-minute buffers around visually refined mid-transit times. To remove instrumental systematics and stellar variability on timescales from days to a month, we applied a Savitzky–Golay filter (A. Savitzky & M. J. E. Golay 1964) with a 12-hour window, resulting in flattened, normalized light curves suitable for transit analysis.

3. TRANSIT MODELING

We employed a customized version of the `Transit Analysis Package` (TAP; J. Z. Gazak et al. 2012) to derive key transit parameters: the mid-transit time T_{mid} , planet-to-star radius ratio R/R_* , transit chord duration τ (defined as the interval between the moments when the center of the planet crosses the stellar limb at ingress and egress), and the impact parameter b (normalized to R_*). The stellar limb darkening was modeled using a quadratic law, with coefficients $u_{1,\text{TESS}}$ and $u_{2,\text{TESS}}$ interpolated from the tables of A. Claret & S. Bloemen (2011) using the stellar parameters from M. J. Hobson et al. (2021). Gaussian priors with widths of 0.1 and 0.2 were applied, following J. A. Patel & N. Espinoza (2022). Residual baseline trends near each transit were removed using second-order polynomials.

TAP was applied to light curve segments centered on each transit, extracted with margins of 2.5τ . In the first fitting pass, all parameters except T_{mid} were linked across transits to determine global values. In a second iteration, we allowed R/R_* , τ , and b to vary per transit to check for potential variability. No significant inter-transit differences were found. In an additional test, $u_{1,\text{TESS}}$ and $u_{2,\text{TESS}}$ were treated as free parameters. While the fitted values remained consistent with theoretical predictions within 1σ , their uncertainties increased by a factor of two. We therefore adopted the literature values for our final modeling.

We explored the parameter space using ten MCMC walkers, each run for 10^6 steps with a 10% burn-in.

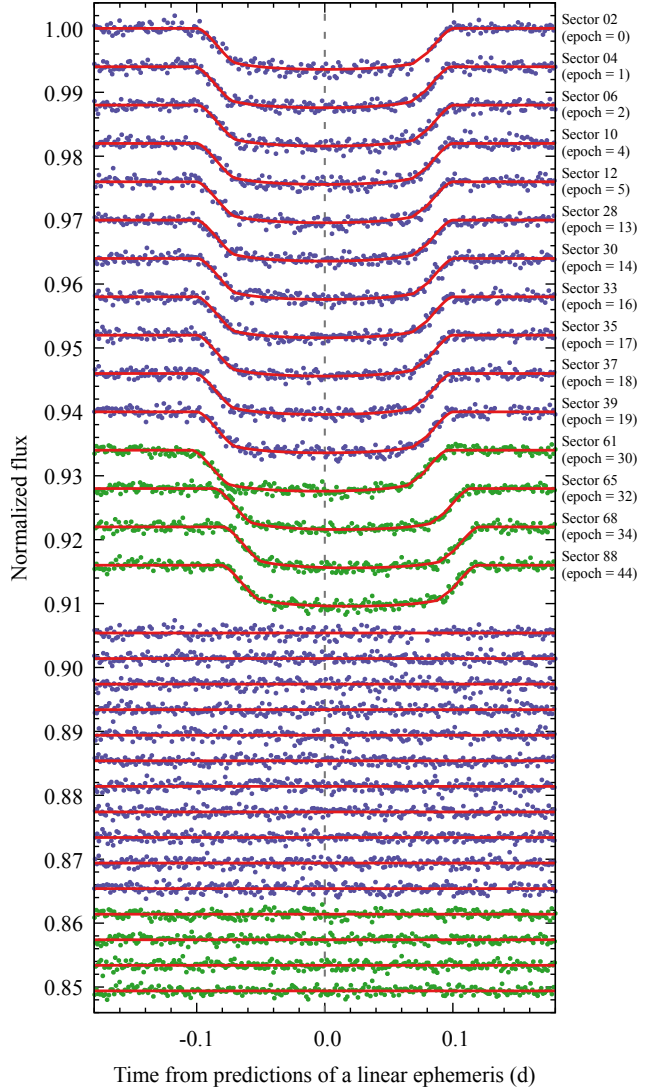


Figure 1. Transit light curves of TOI-201 b observed with TESS. Transits consistent with a linear ephemeris are shown in blue, with predicted mid-transit times marked by the dashed gray line. Transits exhibiting significant timing offsets, particularly those from Sectors 65–88, are plotted in green. Best-fitting models are overlaid in red, with residuals shown below.

The chain convergence was verified with the multivariate Gelman-Rubin statistic and the number of effective samples. Median values and uncertainties were taken from the posterior distributions at the 50th, 15.9th, and 84.1st percentiles. The average transit parameters are listed in Table 1, while individual transit fits are summarized in Table 2. The transit light curves of TOI-201 b, along with best-fitting models and residuals, are shown in Fig. 1.

Our visual inspection of Sector 64 revealed an incomplete transit inconsistent with TOI-201 b. Although

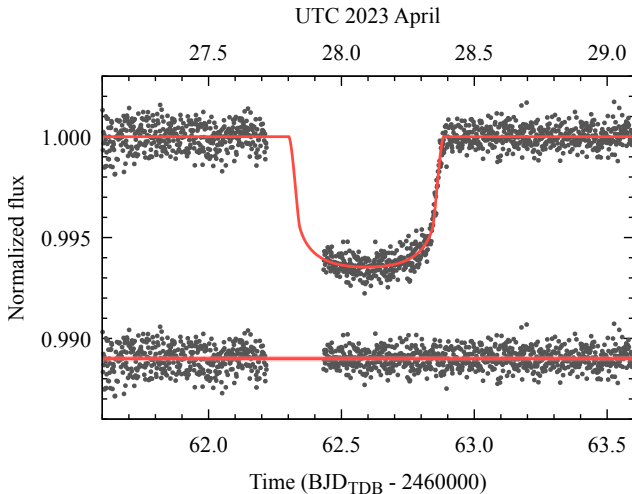


Figure 2. Transit light curve of TOI-201 c detected in TESS Sector 64. The best-fitting model is shown in red, with residuals plotted below.

similar in depth, it exhibited a significantly longer duration—estimated at 10–15 hours. The ingress was missed due to a data gap during the apogee downlink in TESS orbit 136. We attribute this event to a newly identified outer companion, TOI-201 c. This transit was modeled using the same TAP procedure. The resulting fit and residuals are presented in Fig. 2, with parameters included in Table 1.

4. TWO-PLANETARY DYNAMICAL MODEL

To investigate potential gravitational interactions in the TOI-201 system, we analyzed the transit timing behavior of TOI-201 b. Our analysis began by refining the planet’s linear ephemeris using transits from TESS Sectors 2–39. We adopted the standard form:

$$T_{\text{mid},b}(E) = T_{0,b} + P'_b \times E, \quad (1)$$

where E is the transit number counted from a reference epoch. We determined $T_{0,b} = 2458376.05207 \pm 0.00031$ BJD_{TDB} (corresponding to the first TESS-observed transit) and an apparent orbital period of $P'_b = 52.978199 \pm 0.000025$ d. These values were obtained by sampling the posterior probability distribution using an MCMC analysis with 100 chains, each consisting of 10^4 steps and a 10% burn-in.

Figure 3, panel a, shows the timing residuals relative to this refined linear ephemeris. Transits from Sectors 2–39, which align well with the linear model, are marked in blue, while later transits—those from Sectors 61 and 65–88—exhibit significant deviations of up to 30 minutes and are shown in green. A bundle of 50 posterior realizations of the linear ephemeris is overplotted in blue to illustrate its propagated uncertainty. These

deviations from linearity are too large to be attributed to measurement noise and strongly suggest the presence of dynamical perturbations from a second body in the system.

Motivated by these anomalies, we constructed a two-planet dynamical model using the **TTVFast** integrator (K. M. Deck et al. 2014) and the dynamic nested sampling algorithm from the **dynesty** package (J. S. Speagle 2020). The model simultaneously fits TTVs, transit shape parameters, and radial velocity (RV) data. Our observational inputs included the mid-transit times, durations (τ_b), and impact parameters (b_b) for 15 observed transits of TOI-201 b, as well as single measurements of $T_{\text{mid},c}$, τ_c , and b_c for TOI-201 c. These were supplemented with 39 HARPS RV measurements from M. J. Hobson et al. (2021), chosen for their superior precision and longer time coverage (from November 2018 to August 2020). Other RV datasets were not included in the final fit due to their lower quality, with uncertainties comparable to or exceeding the RV amplitude induced by TOI-201 b. We note that including these additional data leaves our results essentially unchanged.

Assuming Gaussian and uncorrelated errors on all input observables, the likelihood function took the form:

$$\log \mathcal{L} = -\frac{1}{2} \sum_i \left[\frac{(\mathcal{O}_i - \mathcal{M}_i)^2}{\sigma_i^2} + \log(2\pi\sigma_i^2) \right], \quad (2)$$

where \mathcal{O}_i and σ_i are the observed values and uncertainties, and \mathcal{M}_i are the corresponding model predictions.

The dynamical model included the following free parameters: the masses M_b and M_c , orbital periods P_b and P_c , eccentricities e_b and e_c , inclinations i_b and i_c , arguments of periastron ω_b and ω_c , and mean anomalies $\theta_{m,b}$ and $\theta_{m,c}$ at a common epoch. The longitude of the ascending node for TOI-201 b was fixed to 0° , establishing the reference for TOI-201 c’s relative node, Ω_c . The model also included RV offset and jitter terms. The stellar mass was fixed at $M_\star = 1.316 M_\odot$ from M. J. Hobson et al. (2021), while the stellar radius R_\star was treated as a free parameter to allow consistent derivation of b and τ from dynamical quantities. Physical consistency was enforced by requiring agreement between the stellar density inferred from each planet’s transit and the value derived from the fixed M_\star and fitted R_\star .

In addition to predicting transit times and radial velocities, **TTVFast** also computes the sky-projected astrometric distance r_{sky} and the sky-projected astrometric velocity v_{sky} , which can be converted into b and τ via the following relations:

$$b = \frac{r_{\text{sky}}}{R_\star}, \quad (3)$$

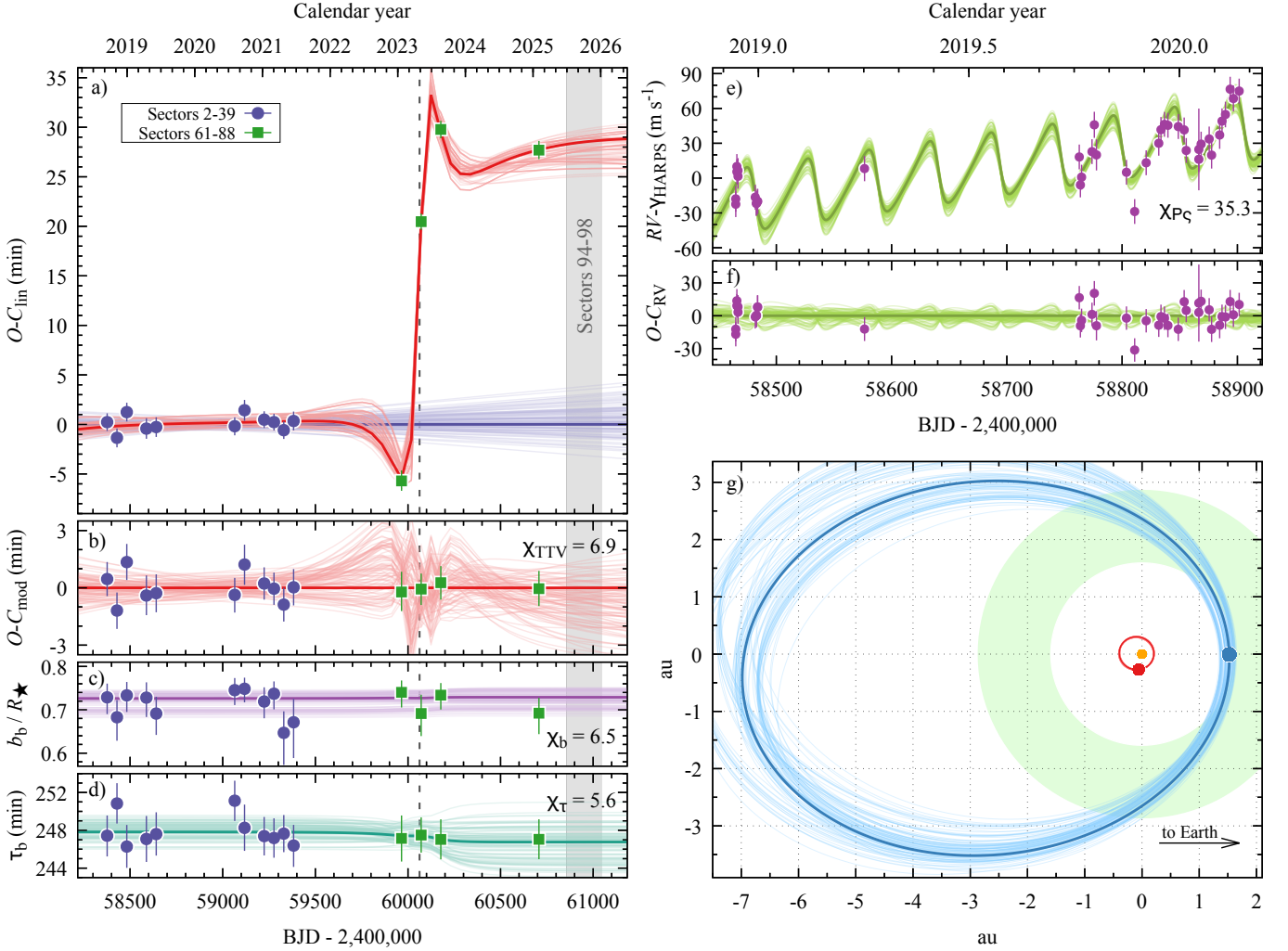


Figure 3. Transit observables for TOI-201 b from the dynamical model. Panel a: Transit timing residuals relative to the refined linear ephemeris, derived using mid-transit times from TESS Sectors 2–39 (blue dots). The thick blue line represents the linear ephemeris propagated to later epochs, where deviations caused by TOI-201 c become apparent. A set of 50 posterior realizations is overplotted to illustrate the uncertainty in this ephemeris. Mid-transit times of TOI-201 b that deviate significantly from the linear prediction are highlighted in green. The best-fitting two-planet dynamical model is shown as a thick red line, with 100 posterior samples overplotted to illustrate model uncertainty. The shaded gray region indicates the window of upcoming TESS observations. The vertical dashed line marks the transit of TOI-201 c. Panel b: Transit timing residuals relative to the best-fitting dynamical model. Panels c and d: Evolution of the impact parameter b_b and transit duration τ_b , respectively, as predicted by the model. Uncertainties are indicated by the ensemble of posterior realizations. Panel e: HARPS RV measurements with the best-fitting two-planet dynamical model overplotted. The RV modulation induced by TOI-201 b is superimposed on a long-term trend caused by TOI-201 c. The residuals are shown in panel f. Panel g: schematic diagram showing the astrocetric architecture of the TOI-201 system. The orbits of planets b and c are shown in red and blue, respectively. Uncertainties are illustrated using 100 posterior samples. Planet positions at the epoch of $T_{\text{mid},c}$ are marked with dots, and the host star is shown as an orange dot. Sizes of all bodies are not to scale. The pale green region indicates the circumstellar habitable zone, using conservative inner and outer boundaries (runaway and maximum greenhouse) computed via Equations (2) and (3) from R. K. Kopparapu et al. (2013).

$$\tau = \frac{2}{v_{\text{sky}}} \sqrt{R_{\star}^2 - r_{\text{sky}}^2}. \quad (4)$$

These expressions link the modeled orbital geometry to observable transit parameters, adding further constraints on the orbital evolution.

We explored the parameter space with multiple runs of dynamic nested sampling, each using 6400 live points. Convergence was reached when the change in log-evidence dropped below $\Delta \ln \mathcal{Z} < 0.001$. To avoid trapping in local maxima, prior grids were imposed on P_c (spanning 2350–9850 d in steps of 200–500 d) and Ω_c

(spanning 0° – 330° in 30° intervals, each within $\pm 20^\circ$). The inclination i_c was explored in two separate regimes: $i_c \leq 90^\circ$ and $i_c \geq 90^\circ$, while i_b was restricted to $i_b \leq 90^\circ$ to avoid degeneracy in i_b and τ_b .

The resulting log-likelihood surface showed clear, distinct maxima for P_c in the 2600–3300 d range, with solutions most strongly clustered around $\Omega_c \approx 0^\circ, 90^\circ, 180^\circ$, and 270° . Among these, configurations near $\Omega_c \approx 0^\circ$ were decisively favored by the Bayesian Information Criterion (BIC), with $\Delta\text{BIC} > 15$ relative to other maxima. The inclination of planet c exhibited a bimodal distribution with distinct peaks at i_c and $180^\circ - i_c$. Although both families of solutions fit the data equally well (with $\Delta\text{BIC} < 2$), the best-fitting model lies within the $i_c < 90^\circ$ regime, and we focus on that branch in the following discussion.

The best-fitting model parameters are reported in Table 1, with uncertainties defined by the 15.9th and 84.1st percentiles of merged posterior samples from all models within $\Delta\text{BIC} < 2$ of the best solution. The convergence of this merged sample was verified qualitatively with visual inspection of the profile likelihood for each model parameter (e.g., E. Agol et al. 2021), which confirmed that the posterior modes correspond to isolated, well-resolved regions of parameter space. TOI-201 c emerges as a super-Jupiter or low-mass brown dwarf ($M_c = 14.2^{+1.0}_{-1.2} M_{\text{Jup}}$) in a highly eccentric ($e_c = 0.643^{+0.009}_{-0.021}$), long-period ($P_c = 7.7^{+1.0}_{-0.6}$ years) orbit. The mutual inclination between the planetary orbits is $i_{bc} = 2.9^{+4.8}_{-4.4}$ degrees, consistent with a coplanar configuration.

Figure 3, panel a, shows the dynamical model’s fit to the transit timing residuals (red line) and 100 posterior realizations. The corresponding residuals are plotted in panel b. Panels c and d show the predicted evolution of b_b and τ_b , respectively. The model predicts only a 0.4% decrease in b_b during the 2023 periastron passage—below current detection limits—and a small, marginally significant change in τ_b of approximately 1 minute. The observed difference in τ_b between pre- and post-2023 transits is 0.5 ± 2.4 minutes, consistent with this prediction. Panels e and f show the RV component of the model and its residuals, respectively, while panel g presents a schematic diagram of the system architecture.

Future TESS observations (Sectors 94–98) are expected to include four additional transits of TOI-201 b. These will reduce uncertainties on τ_b by an estimated 30%, but likely still fall short of definitively resolving the predicted signal.

5. DISCUSSION

TOI-201 c is among the longest-period transiting exoplanets discovered to date, with an orbital period com-

parable to that of K2-311 b (H. A. C. Giles et al. 2018), which orbits an evolved subgiant. Notably, TOI-201 c is the longest-period transiting planet discovered by TESS. What distinguishes it is not only its extreme orbital period, but also the tight constraints on its orbital and physical parameters. Its coexistence with TOI-201 b in a nearly coplanar, dynamically interacting configuration makes the TOI-201 system a rare and valuable laboratory for testing theories of planetary formation, migration, and long-term dynamical evolution.

With a mass of $\sim 14 M_{\text{Jup}}$, TOI-201 c lies near the deuterium-burning threshold traditionally used to distinguish giant planets from brown dwarfs. Its classification depends critically on formation history: if it formed via core accretion, as suggested by its ~ 4 au orbit and the host star’s high metallicity ($[\text{Fe}/\text{H}] = 0.240 \pm 0.036$; M. J. Hobson et al. 2021), it would be considered a planet (K. C. Schlaufman 2018). Its bulk density of $\sim 19 \text{ g cm}^{-3}$ places it firmly on the empirical mass–density sequence of massive exoplanets (A. P. Hatzes & H. Rauer 2015), reinforcing its classification as a high-mass giant planet rather than a stellar brown dwarf.

Despite its long orbital period, the extreme eccentricity of TOI-201 c brings it to within 1.5 au of its host star at periastron, leading to strong irradiation-driven variations over the orbit. Assuming a Bond albedo of 0.3 and full energy redistribution (M. S. Marley et al. 1999), the planet’s orbit-averaged equilibrium temperature (N. B. Cowan & E. Agol 2011) is 169 ± 6 K. However, incident stellar flux swings from 0.05 to $1.1 S_\odot$, periodically bringing the planet into the habitable zone at periastron (see panel g of Fig. 3).

We explored the long-term dynamical evolution of the best-fitting model using the *SWIFT* symplectic integrator (H. F. Levison & M. J. Duncan 1994, 2013), running numerical simulations over 50 kyr with a timestep of 1% of P_b . To assess orbital stability, we computed the chaos indicator D (J. Laskar 1990, 1993) for each planet, based on frequency diffusion across two 25-kyr intervals (e.g., A. C. M. Correia et al. 2005). The resulting values, $\log D_b = -7.0$ and $\log D_c = -10.3$, indicate long-term stability on Gyr timescales. Indeed, in a separate 800-Myr integration—comparable to the system’s estimated age—both planetary orbits remained regular, with no signs of chaotic evolution.

The orbital elements of TOI-201 b show secular modulation under the perturbation of TOI-201 c. Its eccentricity oscillates between 0.12 and 0.32 on a ~ 25 kyr timescale, while the inclination cycles between 87° and 93° over ~ 21 kyr, exhibiting a step-like evolution pattern, triggered by gravitational perturbations from TOI-201 c during its periastron passages. These short-

timescale variations in i_b induce corresponding discrete changes in τ_b . While these individual steps are small—about 1 minute—they accumulate across successive orbits, leading to measurable long-term trends. Transit visibility is likewise modulated: TOI-201 b remains observable during only $\sim 30\%$ of its inclination cycle, with transits expected to cease around the year 3000 and resume approximately 7000 years later. In contrast, transits of TOI-201 c persist throughout its secular cycle, with b_c varying between 0.35 and 0.8 and durations oscillating between 10 and 15 hours. Although TOI-201 c is predicted to exhibit smooth TTVs with an amplitude of approximately 4 days, these occur on a timescale of ~ 3000 years and will remain undetectable in the foreseeable future.

Our dynamical model revises the mass of TOI-201 b upward by approximately 40% compared to the value reported by [M. J. Hobson et al. \(2021\)](#), a discrepancy significant at the $\sim 2\sigma$ level. The difference likely stems from Gaussian process detrending in their adopted model 6, which may partially absorb the RV signal. Our derived RV semi-amplitude K_b agrees more closely with values from their alternative fits: model 3 (single planet, eccentric orbit) and model 5 (eccentric orbit with a quadratic trend).

We also explored the dynamical role of TOI-201.02, a candidate inner planet detected via transits. Using the mass–radius relation recently refined by [S. Müller et al. \(2024\)](#), we estimate its mass to be $\sim 5 M_\oplus$. We introduced a planet of this mass into our dynamical model to assess its interactions with the two confirmed giants. The test body remains dynamically decoupled from TOI-201 c on decadal timescales, but experiences TTVs induced by TOI-201 b, with a characteristic period of ~ 900 days and amplitudes reaching ~ 5 minutes. These TTVs would be challenging to detect due to the planet’s shallow transit depth and current observational limitations. Conversely, the gravitational influence of TOI-201.02 on TOI-201 b results in TTVs of less than ~ 20 seconds, well below existing detection thresholds.

6. CONCLUSIONS

We presented a comprehensive dynamical model of the TOI-201 system, based on a joint analysis of transit timing variations, radial velocity measurements, and the newly observed transit of the outer companion. The detection of TOI-201 c was initially inferred from the high-amplitude TTV signal it induces on TOI-201 b—an uncommon case in which a long-period transiting planet was first revealed through its dynamical imprint. Its subsequent transit detection by TESS confirms the pre-

diction and provides a crucial observational anchor for the system’s architecture.

TOI-201 c follows an eccentric ~ 8 -year orbit and has a mass of $\approx 14 M_{\text{Jup}}$, placing it near the boundary between massive planets and brown dwarfs. Its nearly coplanar orbit with TOI-201 b, along with the high metallicity of the host star, supports a formation pathway via core accretion. Long-term numerical integrations confirm the system’s stability over gigayear timescales and predict that transits of TOI-201 b will vanish within the next few millennia due to secular oscillations in orbital inclination.

As one of the longest-period transiting planets with precisely constrained properties, TOI-201 c provides a rare opportunity to probe the architecture, formation, and long-term evolution of giant planetary systems. TOI-201 thus emerges as a valuable natural laboratory for testing theories of planet–planet interactions, orbital dynamics, and the transition between planetary and substellar regimes. Continued observations—particularly with future TESS coverage and radial velocity monitoring—will further refine our understanding and may reveal additional dynamical features in this remarkable system.

ACKNOWLEDGMENTS

We thank the anonymous referee for their constructive and insightful comments, which helped improve the quality and clarity of this Letter. GM acknowledges the financial support from the National Science Centre, Poland, through grant no. 2023/49/B/ST9/00285. This paper includes data collected with the TESS mission, obtained from the MAST data archive at the Space Telescope Science Institute (STScI). These data can be accessed at [doi: 10.17909/t9-yk4w-zc73](https://doi.org/10.17909/t9-yk4w-zc73) ([MAST Team 2021](#)). Funding for the TESS mission is provided by the NASA Explorer Program. STScI is operated by the Association of Universities for Research in Astronomy, Inc., under NASA contract NAS 5-26555. This research made use of [Lightkurve](#), a Python package for Kepler and TESS data analysis ([Lightkurve Collaboration et al. 2018](#)). This research has made use of the SIMBAD database and the VizieR catalogue access tool, operated at CDS, Strasbourg, France, and NASA’s Astrophysics Data System Bibliographic Services.

AUTHOR CONTRIBUTIONS

WL reduced the photometric observations from Sectors 1–68 and conducted the preliminary TTV analysis. GM carried out the remaining research work, including further data analysis and interpretation.

Table 1. Systemic parameters for TOI-201

Parameter	Units	Prior	Value	Source
TOI 201 b				
Orbital period, P_b	d	$\mathcal{U}(52.96, 52.99)$	$52.977946^{+0.000031}_{-0.000040}$	TTVFast dynamical model
Orbital eccentricity, e_b	—	$\mathcal{U}(0.0, 0.5)$	$0.318^{+0.020}_{-0.022}$	TTVFast dynamical model
Orbital inclination, i_b	°	$\mathcal{U}(88, 90)$	$88.747^{+0.029}_{-0.032}$	TTVFast dynamical model
Argument of periastron, ω_b	°	$\mathcal{U}(0, 360)$	$81.3^{+4.4}_{-5.6}$	TTVFast dynamical model
Longitude of the ascending node, Ω_b	°	fixed	0.0	TTVFast dynamical model
Mean anomaly, $\theta_{m,b}$	°	$\mathcal{U}(180, 360)$	$323.2^{+2.8}_{-2.3}$	TTVFast dynamical model
Radius ratio, R_b/R_\star	—	—	0.07919 ± 0.00028	TAP transit model
Transit impact parameter, b_b	—	—	$0.729^{+0.011}_{-0.010}$	TAP transit model
Transit duration, τ_b	min	—	$247.16^{+0.89}_{-0.87}$	TAP transit model
Total transit duration, $\tau_{14,b}$	min	—	287.4 ± 1.2	derived
Mass, M_b	M_{Jup}	$\mathcal{U}(0.1, 0.9)$	$0.580^{+0.070}_{-0.061}$	TTVFast dynamical model
Radius, R_b	R_{Jup}	—	$1.055^{+0.014}_{-0.009}$	derived
Density, ρ_b	g cm^{-3}	—	$0.654^{+0.081}_{-0.074}$	derived
Semi-major axis, a_b	au	—	0.3026 ± 0.0021	derived
RV amplitude, K_b	m s^{-1}	—	$27.6^{+3.3}_{-2.9}$	derived
TOI 201 c				
Orbital period, P_c	d	$\mathcal{U}(2350, 9850)$	2800^{+360}_{-210}	TTVFast dynamical model
Orbital eccentricity, e_c	—	$\mathcal{U}(0.5, 0.9)$	$0.643^{+0.009}_{-0.021}$	TTVFast dynamical model
Orbital inclination, i_c	°	$\mathcal{U}(89, 91)$	$89.896^{+0.030}_{-0.017}$	TTVFast dynamical model
Argument of periastron, ω_c	°	$\mathcal{U}(0, 360)$	$95.2^{+3.2}_{-7.2}$	TTVFast dynamical model
Longitude of the ascending node, Ω_c	°	$\mathcal{U}(-20, 350)$	$2.7^{+5.2}_{-4.8}$	TTVFast dynamical model
Mean anomaly, $\theta_{m,c}$	°	$\mathcal{U}(0, 360)$	115^{+27}_{-19}	TTVFast dynamical model
Radius ratio, R_c/R_\star	—	—	$0.07449^{+0.00087}_{-0.00091}$	TAP transit model
Transit impact parameter, b_c	—	—	$0.44^{+0.13}_{-0.23}$	TAP transit model
Transit duration, τ_c	min	—	771^{+66}_{-40}	TAP transit model
Total transit duration, $\tau_{14,c}$	min	—	838^{+71}_{-41}	derived
Transit mid-point, $T_{\text{mid},c}$	BJD_{TDB}	—	$2460062.593^{+0.014}_{-0.024}$	TAP transit model
Mass, M_c	M_{Jup}	$\mathcal{U}(1, 40)$	$14.2^{+1.0}_{-1.2}$	TTVFast dynamical model
Radius, R_c	R_{Jup}	—	$0.993^{+0.017}_{-0.014}$	derived
Density, ρ_c	g cm^{-3}	—	$19.2^{+1.0}_{-1.2}$	derived
Semi-major axis, a_c	au	—	$4.28^{+0.36}_{-0.21}$	derived
RV amplitude, K_c	m s^{-1}	—	221^{+16}_{-18}	derived
Common				
Mutual orbital inclination, i_{bc}	°	—	$2.9^{+4.8}_{-4.4}$	derived
Stellar mass, M_\star	M_\odot	—	1.316 ± 0.027	M. J. Hobson et al. (2021)
Stellar radius, R_\star	R_\odot	$\mathcal{U}(1.2, 1.5)$	$1.339^{+0.017}_{-0.011}$	TTVFast dynamical model
Linear LD coefficient, $u_{1,\text{TESS}}$	—	$\mathcal{N}(0.23, 0.10)$	0.211 ± 0.023	TAP transit model
Quadratic LD coefficient, $u_{2,\text{TESS}}$	—	$\mathcal{N}(0.32, 0.20)$	0.267 ± 0.036	TAP transit model
HARPS barycentric RV, γ_{HARPS}	m s^{-1}	$\mathcal{U}(16770, 17070)$	16905^{+11}_{-17}	TTVFast dynamical model
HARPS RV jitter, $\sigma_{\text{jitter,HARPS}}$	m s^{-1}	$\mathcal{U}(0, 50)$	$10.5^{+3.1}_{-1.6}$	TTVFast dynamical model
Goodness of fit, χ^2	—	—	54.4	TTVFast dynamical model
Number of degrees of freedom, N_{dof}	—	—	71	TTVFast dynamical model

NOTE—Priors are given for free parameters of the dynamical fit and for the LD coefficients in transit light curves modeling. The orbital parameters are given in the astrometric reference system for epoch $\text{BJD}_{\text{TDB}} 2,458,158.087205$.

Table 2. Parameters for individual transits of TOI-201 b

Sector	Date	E	T_{mid} (BJD _{TDB})	R_b/R_\star	b_b/R_\star	τ_b (min)	χ^2	N_{dof}	\hat{R}_z	N_{ess}
2	2018.7029	0	2458376.05223 ^{+0.00062} _{-0.00062}	0.0800 ^{+0.0010} _{-0.0010}	0.729 ^{+0.032} _{-0.039}	247.4 ^{+2.1} _{-2.2}	1081.7	829	1.018	6472
4	2018.8480	1	2458429.02932 ^{+0.00066} _{-0.00067}	0.0780 ^{+0.0011} _{-0.0011}	0.683 ^{+0.040} _{-0.054}	250.8 ^{+2.2} _{-2.1}	1348.3	853	1.016	6593
6	2018.9932	2	2458482.00932 ^{+0.00066} _{-0.00065}	0.0794 ^{+0.0011} _{-0.0011}	0.733 ^{+0.031} _{-0.038}	246.3 ^{+2.3} _{-2.2}	1362.9	855	1.020	6804
10	2019.2835	4	2458587.96457 ^{+0.00073} _{-0.00071}	0.0797 ^{+0.0012} _{-0.0012}	0.728 ^{+0.035} _{-0.045}	247.1 ^{+2.4} _{-2.4}	1518.3	854	1.013	6758
12	2019.4286	5	2458640.94287 ^{+0.00068} _{-0.00069}	0.0792 ^{+0.0012} _{-0.0012}	0.691 ^{+0.039} _{-0.049}	247.6 ^{+2.3} _{-2.3}	1182.9	803	1.013	6904
28	2020.5882	13	2459064.76853 ^{+0.00062} _{-0.00064}	0.0788 ^{+0.0010} _{-0.0010}	0.745 ^{+0.028} _{-0.034}	251.1 ^{+2.1} _{-2.1}	1075.5	854	1.026	6374
30	2020.7329	14	2459117.74784 ^{+0.00072} _{-0.00074}	0.0793 ^{+0.0011} _{-0.0011}	0.748 ^{+0.026} _{-0.031}	248.3 ^{+2.5} _{-2.4}	1358.5	854	1.010	7819
33	2021.0225	16	2459223.70358 ^{+0.00059} _{-0.00059}	0.0792 ^{+0.0010} _{-0.0010}	0.719 ^{+0.033} _{-0.039}	247.4 ^{+2.0} _{-2.0}	1117.1	854	1.017	6271
35	2021.1676	17	2459276.68161 ^{+0.00058} _{-0.00059}	0.0794 ^{+0.0010} _{-0.0010}	0.737 ^{+0.028} _{-0.036}	247.2 ^{+2.1} _{-2.1}	1075.2	855	1.020	6411
37	2021.3128	18	2459329.65924 ^{+0.00061} _{-0.00062}	0.0777 ^{+0.0011} _{-0.0012}	0.647 ^{+0.050} _{-0.074}	247.6 ^{+2.0} _{-2.0}	1244.8	854	1.015	6194
39	2021.4579	19	2459382.63808 ^{+0.00066} _{-0.00066}	0.0780 ^{+0.0013} _{-0.0014}	0.671 ^{+0.054} _{-0.083}	246.4 ^{+2.2} _{-2.3}	1293.1	840	1.016	5998
61	2023.0545	30	2459965.39407 ^{+0.00074} _{-0.00069}	0.0794 ^{+0.0011} _{-0.0012}	0.740 ^{+0.027} _{-0.035}	247.1 ^{+2.4} _{-2.4}	1041.4	855	1.013	7131
65	2023.3448	32	2460071.36864 ^{+0.00057} _{-0.00058}	0.0779 ^{+0.0011} _{-0.0011}	0.691 ^{+0.043} _{-0.052}	247.5 ^{+1.9} _{-1.9}	890.8	855	1.035	5897
68	2023.6352	34	2460177.33151 ^{+0.00060} _{-0.00062}	0.0796 ^{+0.0010} _{-0.0010}	0.734 ^{+0.028} _{-0.033}	247.0 ^{+2.1} _{-2.1}	1115.8	854	1.017	6942
88	2025.0839	44	2460707.11204 ^{+0.00065} _{-0.00063}	0.0780 ^{+0.0011} _{-0.0012}	0.692 ^{+0.035} _{-0.048}	247.0 ^{+2.1} _{-2.1}	1069.8	855	1.012	6811

NOTE—Date is a calendar year in decimal format. E is a transit number counted from the reference epoch given by Eq. 1. N_{dof} is the number of degrees of freedom. \hat{R}_z is the multivariate Gelman-Rubin statistic. N_{ess} is the number of effective samples.

Facility: TESS

Software: Lightkurve ([Lightkurve Collaboration et al. 2018](#)), Transit Analysis Package (J. Z. Gazak et al.

2012), TTVFast (K. M. Deck et al. 2014), dynesty (J. S. Speagle 2020), SWIFT (H. F. Levison & M. J. Duncan 2013)

REFERENCES

- Agol, E., Dorn, C., Grimm, S. L., et al. 2021, PSJ, 2, 1, doi: [10.3847/PSJ/abd022](#)
- Claret, A., & Bloemen, S. 2011, A&A, 529, A75, doi: [10.1051/0004-6361/201116451](#)
- Correia, A. C. M., Udry, S., Mayor, M., et al. 2005, A&A, 440, 751, doi: [10.1051/0004-6361:20042376](#)
- Cowan, N. B., & Agol, E. 2011, ApJ, 726, 82, doi: [10.1088/0004-637X/726/2/82](#)
- Deck, K. M., Agol, E., Holman, M. J., & Nesvorný, D. 2014, ApJ, 787, 132, doi: [10.1088/0004-637X/787/2/132](#)
- Dong, J., Huang, C. X., Dawson, R. I., et al. 2021, ApJS, 255, 6, doi: [10.3847/1538-4365/abf73c](#)
- Gazak, J. Z., Johnson, J. A., Tonry, J., et al. 2012, Advances in Astronomy, 2012, 697967, doi: [10.1155/2012/697967](#)
- Giles, H. A. C., Osborn, H. P., Blanco-Cuaresma, S., et al. 2018, A&A, 615, L13, doi: [10.1051/0004-6361/201833569](#)
- Guerrero, N. M., Seager, S., Huang, C. X., et al. 2021, ApJS, 254, 39, doi: [10.3847/1538-4365/abefel](#)
- Hatzes, A. P., & Rauer, H. 2015, ApJL, 810, L25, doi: [10.1088/2041-8205/810/2/L25](#)
- Hobson, M. J., Brahm, R., Jordán, A., et al. 2021, AJ, 161, 235, doi: [10.3847/1538-3881/abeaa1](#)
- Houk, N., & Cowley, A. P. 1975, University of Michigan Catalogue of two-dimensional spectral types for the HD stars. Volume I. Declinations -90_ to -53_f0.
- Kipping, D. 2021, MNRAS, 500, 1851, doi: [10.1093/mnras/staa3398](#)
- Kopparapu, R. K., Ramirez, R., Kasting, J. F., et al. 2013, ApJ, 765, 131, doi: [10.1088/0004-637X/765/2/131](#)
- Laskar, J. 1990, Icarus, 88, 266, doi: [10.1016/0019-1035\(90\)90084-M](#)
- Laskar, J. 1993, Physica D Nonlinear Phenomena, 67, 257, doi: [10.1016/0167-2789\(93\)90210-R](#)
- Levison, H. F., & Duncan, M. J. 1994, Icarus, 108, 18, doi: [10.1006/icar.1994.1039](#)
- Levison, H. F., & Duncan, M. J. 2013,, Astrophysics Source Code Library, record ascl:1303.001
- Lightkurve Collaboration, Cardoso, J. V. d. M., Hedges, C., et al. 2018, <http://ascl.net/1812.013>
- Loboda, W. 2024, Master’s thesis, Nicolaus Copernicus University, Toruń, Poland. <https://apd.umk.pl/diplomas/148300/>
- Marley, M. S., Gelino, C., Stephens, D., Lunine, J. I., & Freedman, R. 1999, ApJ, 513, 879, doi: [10.1086/306881](#)
- MAST Team. 2021, STScI/MAST, doi: [10.17909/T9-YK4W-ZC73](#)
- Montalto, M., Borsato, L., Granata, V., et al. 2020, MNRAS, 498, 1726, doi: [10.1093/mnras/staa2438](#)
- Müller, S., Baron, J., Helled, R., Bouchy, F., & Parc, L. 2024, A&A, 686, A296, doi: [10.1051/0004-6361/202348690](#)
- Patel, J. A., & Espinoza, N. 2022, AJ, 163, 228, doi: [10.3847/1538-3881/ac5f55](#)
- Ricker, G. R., Winn, J. N., Vanderspek, R., et al. 2015, Journal of Astronomical Telescopes, Instruments, and Systems, 1, 014003, doi: [10.1117/1.JATIS.1.1.014003](#)
- Savitzky, A., & Golay, M. J. E. 1964, Analytical Chemistry, 36, 1627, doi: [10.1021/ac60214a047](#)
- Schlaufman, K. C. 2018, ApJ, 853, 37, doi: [10.3847/1538-4357/aa961c](#)
- Speagle, J. S. 2020, MNRAS, 493, 3132, doi: [10.1093/mnras/staa278](#)